MONITORING DYNAMIC CALCIUM HOMEOSTASIS ALTERATIONS BY T_1-WEIGHTED AND T_1-MAPPING CARDIAC MANGANESE-ENHANCED MRI (MEMRI) IN A MURINE MYOCARDIAL INFARCTION MODEL

A Thesis
Presented to
The Academic Faculty

By

Benjamin J Waghorn

In Partial Fulfillment
Of the Requirements for the Degree
Master of Science in Medical Physics

Georgia Institute of Technology

May 2009

Monitoring Dynamic Calcium Homeostasis Alterations by T_1-Weighted and T_1-Mapping Cardiac Manganese-Enhanced MRI (MEMRI) in a Murine Myocardial Infarction Model

Approved by:

Dr. Tom C.-C. Hu
Department of Radiology
Medical College of Georgia

Dr. Farzad Rahnema
Nuclear and Radiological Engineering
and Medical Physics Programs
Georgia Institute of Technology

Dr. Chris Wang
Nuclear and Radiological Engineering
and Medical Physics Programs
Georgia Institute of Technology

Dr. Nathan Yanasak
Department of Radiology
Medical College of Georgia

Date Approved: September 24, 2008

TABLE OF CONTENTS

LIST OF TABLES

LIST OF FIGURES

LIST OF SYMBOLS AND ABBREVIATIONS

ΔR_1 – Defined as (post-$MnCl_2$ infusion R_1) – (pre-$MnCl_2$ infusion R_1)

BW – "Body Weight", referencing the entire body weight of the mouse subject

ECG - "Electrocardiogram"

FOV – "Field of View"

GEFC – "Gradient Echo Flow Compensation" pulse sequence

ICP-MS – "Inductively coupled plasma-mass spectrometry"

Inter-TE – Echo time in Look-Locker sequence following small flip angle excitation

Inversion time/interval – Delay post adiabatic inversion before small flip angle excitation/ delay between subsequent excitations

LAD – "Left Anterior Descending" coronary artery

LV – "Left Ventricle"

LV Wall – "Left Ventricular free wall"

MEMRI – "Manganese-enhanced magnetic resonance imaging"

MI – "Myocardial infarction"

MnDPDP –"Manganese-Dipyridoxyl Diphosphate"

R_1 – Tissue relaxation rate, defined as $1/T_1$

RV – "Right Ventricle"

ROI – "Region of Interest"

SD – "Standard Deviation"

TE – "Echo time"

TR – "Repetition time"

SUMMARY

Manganese has been used as a T_1-weighted MRI contrast agent in a variety of applications. Because manganese ions (Mn^{2+}) enter viable myocardial cells via voltage gated calcium channels, manganese-enhanced MRI (MEMRI) is sensitive to the viability and the inotropic state of the heart. In spite of the established importance of calcium regulation in the heart both prior to, and following, myocardial injury, monitoring strategies to assess calcium homeostasis in affected cardiac tissues are limited. This study implements a T_1-mapping method to obtain quantitative information both dynamically and over a range of $MnCl_2$ infusion doses. In order to optimize the current manganese infusion protocols, both dose dependent and temporal washout studies were performed. A non-linear relationship between infused $MnCl_2$ solution dose and increase in left ventricular free wall relaxation rate (ΔR_1) was observed. Control mice also exhibited significant manganese clearance over time, with approximately 50% decrease of ΔR_1 occurring in just 2.5 hours. The complicated efflux time dependence possibly suggests multiple efflux mechanisms. Using the measured relationship between infused $MnCl_2$ and ΔR_1, absolute Mn concentration ICP-MS data analysis provided a means to estimate the absolute heart Mn concentration *in vivo*. We have shown that this technique has the sensitivity to observe or monitor potential Ca^{2+} handling alterations *in vivo* due to the physiological remodeling following myocardial infarction. Left ventricular free wall ΔR_1 values were significantly lower ($P = 0.005$) in the adjacent zone, surrounding the injured myocardial tissue, than healthy left ventricular free wall tissue. This inferred reduction in Mn concentration can be used to estimate potentially salvageable myocardium *in vivo* for future therapeutic treatment or evaluation of disease progression.

CHAPTER 1

INTRODUCTION

Intracellular calcium is a central regulator of cardiac contractility and viability (1). Calcium (Ca^{2+}) entry through L-type Ca^{2+} channels into cardiac myocytes is known to be the initiating event of the excitation-contraction coupling process (2,3). Calcium entering cells during each action potential must be pumped out of the cell to maintain composition of the cytosol at a steady state. There are two known mechanisms to remove Ca^{2+} from cardiac cells (4), either via the sodium-calcium exchanger (NCX), or via the plasma membrane Ca^{2+}-ATPase (PMCA) (5).

Alterations in myocyte Ca^{2+} handling appear to be centrally involved in the dysfunctional characteristics of the failing heart (6). It has been demonstrated that the principle cause of diminished cardiac performance in the failing heart is due to abnormal intracellular Ca^{2+} handling impairing cardiomyocyte contractility (7,8). During ischemia the sodium-hydrogen exchange mechanism can lead to intracellular sodium overload. This in turn leads to reduced calcium efflux and/or increased calcium influx via the sodium-calcium exchanger mechanism, resulting in intracellular calcium overload (9). Cell death can result from one of several mechanisms following elevations in intracellular calcium concentration. Examples of these mechanisms include protease activation, membrane rupture, cell contracture, and gap junction dysfunction (9,10).

Following myocardial infarction there is progressive myocardial remodeling characterized by left ventricular dilation, contractile dysfunction and myocyte hypertrophy. There are also altered expressions of contractile, calcium-handling, and

extracellular matrix proteins (11). Similarly, myocardial ischemia appears to have significant negative effects both on acute and chronic cardiac remodeling and on damage to other organs, including the vascular endothelium (12,13), kidney (14), skeletal muscle (15,16), and brain (17).

In spite of this established importance of calcium regulation in the heart both prior to, and following, myocardial injury, monitoring strategies to assess calcium homeostasis in affected cardiac tissue are limited. In addition, there are currently no *in vivo* techniques available to study calcium fluxes dynamically over the myocardium. This present study proposes using a T_1-mapping manganese-enhanced MRI technique, with the goal of studying changes in calcium uptake due to myocardial injury in both the myocardial infarction injury site and also in the adjacent zone, surrounding the infarcted region. Such a technique could allow for identification of potentially salvageable myocardium and for differentiation between ischemic, hibernating and stunned myocardium.

1.1 Manganese (Mn^{2+}) as an MRI contrast agent

One potential technique for assessing intracellular calcium is to use a surrogate marker with a comparable ionic radius, such as manganese (Mn^{2+}). Mn^{2+} is an excellent candidate due to its similar chemical properties to calcium; additionally, its shortening of the T_1 relaxation time allows it to serve as an MR contrast agent (18,19). As a result of these chemical properties, Mn^{2+} has the potential to enter viable myocardium via voltage gated calcium channels (20-22), accumulating in the myocytes in an additive fashion

(23,24). These factors combined make Mn^{2+} a useful molecular agent for the study of calcium flux.

In its ionic form, Mn^{2+}, along with other elements from the transition metals and the lanthanide series, exacts a dramatic effect on relaxation properties of water. There are multiple components that compromise the MRI signal following interaction of these ions with excited ^{1}H nuclei. The longitudinal relaxation time, T_1, of the ^{1}H nuclei can be shortened following interaction of the ionic dipoles with the nuclear ^{1}H dipole. The magnitude of this interaction depends on the approach distance between ^{1}H and the ion, which may be large and lead to a small interaction if the ion is part of a larger molecule, such as deoxyhaemoglobin (deoxyHb). The duration of the coupling between the ^{1}H and ionic dipoles, the correlation time, also affects the magnitude of the dipole-dipole interaction. If the ion is not chelated, as is the case with $MnCl_2$ used in this study, it will have a wide range of rotational velocities compared to the excitation frequency of ^{1}H, so the dipole-dipole interaction will be weaker.

For suitable rotational rates, the correlation time will depend on the electron spin relaxation time of the agent (25), where slower electronic relaxation results in greater coupling of the dipoles. Electron spin relaxation times for ionic Mn^{2+} and Gd^{3+} are relatively slow, in the range of $10^{-8} – 10^{-10}$ seconds (26,27).

Mn^{2+}, with a relatively long spin relaxation time, will tend to stimulate spin-flip transitions effectively and is useful for enhancing contrast positively on T_1-weighted images. At higher concentrations, Mn^{2+} is also useful for increasing T_2 relaxation (28). The use of Mn^{2+} to produce shortening of the spin-lattice relaxation time, T_1, was

proposed soon after the conception of using NMR for radiological imaging. In 1973 Lauterbur (29) used Mn^{2+} to shorten T_1 in a pure water sample.

1.2 Manganese-enhanced MRI (MEMRI)

Alterations in myocyte Ca^{2+} regulation may be critical for both the mechanical dysfunction and the arrhthmogenesis associated with congestive heart failure (30,31). Recent advances have improved the feasibility of studying ischemic heart disease with MRI (32). MR contrast agents can be applied in a variety of ways to improve MRI sensitivity for detecting and assessing injured myocardium, and have the potential to be used to detect regional differences in cellular viability within the injured heart. Contrast enhanced perfusion MRI has been used to explore disturbances in both large (angiography) (33) and small (myocardial perfusion) (34) coronary arteries. It is known that the size of the abnormal signal area on Gd-enhanced T_1-weighted MRI correlates well with infarct area (35). However, the size of the nonperfused area on first-pass perfusion images is often smaller than the final infarct area. Therefore, there is a need to obtain other measures of cell viability.

The application of Mn^{2+} contrast enhancement to cardiac MRI, either in the form of paramagnetic free manganese (e.g. $MnCl_2$), or in a chelated form (e.g. manganese dipyridoxyl diphosphate, MnDPDP), allows for the potential monitoring of calcium dynamics, of particular importance in the infarcted heart. Chelation of the paramagnetic ions decrease their rotational velocity and increase the correlation time, both beneficial in increasing T_1 relaxation. However, chelates also alter the approach distance, decreasing

the contrast agent's effect on T_1. In order to achieve the same relaxation effects as free ions, larger doses of the chelate need to be administered. A valuable added benefit of using a chelate is that, for less chemically-reactive but toxic metals such as Gd^{3+} and Mn^{2+}, the chelated complex is excreted from the body within a timescale that greatly decreases the toxic side effects. However, the slow release of Mn^{2+} from chelates, as compared to free ions, make the quantitative study of Mn^{2+} influx rates more complicated.

Manganese-enhanced MRI (MEMRI) has been employed in a wide range of biological studies including the study of neuronal activity (36-38), function (39,40), plasticity (41), and the neural circuitry involved in more complex cognitive and emotional processes (42). Recently it has also been applied to studying *in vivo* axonal transport rates in Alzheimer's disease models (43,44). MEMRI has been used in other areas to label lymphocytes and B-cells (45) and to detect beta-cell activation (46).

Additionally, MEMRI has been used to detect cell viability in the ischemic heart (47-49). A study to assess whether normal myocardial tissue can be differentiated from infarcted tissue using contrast agent Mn-DPDP has been conducted in rats (50). Infusion of various doses of the Mn^{2+} chelate demonstrated that Mn^{2+} was retained in the viable myocardium, but was shown to have rapid clearance from the infarcted region. This demonstrated the ability of the contrast agent to differentiate infarcted tissue from viable tissue. Similarly, in its free paramagnetic form $MnCl_2$ has been shown to demarcate infarcted zones in mice (51) and dogs (52).

More recently work has been completed studying the relaxation enhancing properties of MnDPDP in the human myocardium (53). In this particular study by Skjold

et al., R_1 measurements were calculated for the myocardium of fifteen healthy patients using an inversion recovery (IR) turbo fast low-angle shot (FLASH) sequence, both before and at various time points post i.v. MnDPDP injection. Left ventricular wall R_1 values increased on average 37% one hour following a MnDPDP dose of 5 μmol/kg, the clinical liver dose. This elevation remained for approximately two hours, before a gradual decline lasting over 24 hours. Varying the dose of MnDPDP injections did not cause the R_1 values to increase linearly.

Following this work, Skjold et al. (47) performed a study on patients with recent myocardial infarction. The aim was to see if regions of the left ventricular wall would show signs of reduced R_1 compared to healthy myocardial tissue after a low dose of MnDPDP. The results showed that reduced wall thickening at the infarction site was associated with reduced contrast enhancement. In contrast, the remote regions showed larger increases in R_1. This is most likely due to the selective and slow Mn accumulation in viable myocytes. Conclusions drawn from this work suggest that the demarcation of infarcted myocardial regions is possible with manganese-based MRI contrast. The combination of low doses of MnDPDP with R_1 mapping techniques can reliably identify infarcted regions. One potential advantage of using Mn^{2+} over Gd^{3+} in contrast enhanced studies is that Mn^{2+} could allow for the study of calcium fluxes. Also, Mn^{2+} could have the sensitivity to detect changes in calcium fluxes, not only in the infarcted region but also in the adjacent zone surround the MI site.

Mn^{2+} infusion in mice has been shown to lead to significant signal enhancement in T_1-weighted cardiac MRI (23). It has also been demonstrated that MEMRI is sensitive to changes in inotropy (23), consistent with the model that Mn^{2+}-induced enhancement of

cardiac signal can be used to detect changes in the rate of calcium influx into the heart. While an essential element for the normal physiological functioning in all animal species, with an estimated safe and adequate daily dietary intake (ESADDI) of 2 – 5 mg Mn/day in adults (54), at high concentrations Mn^{2+} is know to be cardiotoxic (55). Previously, a dose-dependent study (23) determined a range of Mn^{2+} infusion doses that result in large signal enhancement without affecting the left ventricular ejection fraction or heart rate.

1.3 T_1-Mapping Cardiac MEMRI in the study of calcium homeostasis alteration

In order to determine the relationship between the $MnCl_2$ infusion dose and the calculated absolute tissue relaxation times due to Mn^{2+} uptake in murine cardiac myocytes, a quantitative imaging technique is required.

T_1-mapping protocols provide such a quantitative technique, allowing for estimations of absolute T_1 values. Experiments aimed to measure tissue T_1 and T_2 relaxation times were conducted as early as 1971, where discriminations between normal tissue and malignant tumor specimens were discerned from their relaxation times (56). In the late 1970's Mansfield et al. extended these techniques to imaging biological structures (57,58).

Quantitative MEMRI T_1-mapping has been applied to numerous fields, for example MEMRI T_1-mapping has been used to improve neuronal tract tracing techniques (59). In neuronal tract tracing Mn^{2+} causes a wide range of T_1 changes, varying from short T_1 values at the injection site, to longer values in more distant regions. In this particular study Chuang et al. (59) used a Look-Locker T_1-mapping protocol that

displayed the sensitivity to detect the full range of T_1 values with full brain coverage in a reasonable time. It was concluded that the use of quantitative techniques in MEMRI should allow for the study of more extensive pathways, and should allow for administration of lower Mn^{2+} doses.

T_1-mapping has also been applied to the study of the common neuropsychiatric condition hepatic encephalopathy (HE) (60). Within clinically relevant acquisition times significant correlations between the change in T_1, due to deposition of manganese, and HE severity have been shown in the globus pallidus, the caudate nucleus, and the posterior limb of the internal capsule.

In many MEMRI experiments there are a large range of T_1 values within the field of view (FOV), such as those experienced in the mouse brain following systemic administration of $MnCl_2$ (61). T_1 weighted images need to be optimized in order to detect a specific range of T_1 values. However, it is not typically possible to detect the complete range of T_1 values using just one protocol, and acquisition of multiple images is required. Similarly, small changes in T_1 values could provide important information that T_1 weighted imaging techniques do not have the sensitivity to detect. Utilizing a quantitative technique provides a greater sensitivity to a wide range of T_1 changes, and also allows for reduced doses of Mn^{2+} to be administered. By reducing the dose, potential cardiotoxic and neurotoxic effects caused by high levels of Mn^{2+} can be minimized. Spin-echo inversion recovery (IR) techniques can be used to estimate T_1 values, but the long echo times (TE) required in this sequence cannot be used with the relatively fast heart rate of the mouse.

The goal of using a quantitative technique within this study is to estimate the delivery of Mn^{2+} to viable myocardium *in vivo*, with applications to assess regional Mn^{2+} handling alterations in a myocardial infarction model. In 1970, a commonly used method to calculate T_1 values was introduced by Look and Locker (62,63), whereby T_1 relaxation times can be estimated using a periodic train of excitation pulses, sampling multiple time points during signal recovery. This method can significantly reduce scanning time without sacrificing accuracy, and has been shown to have almost the same efficiency as the spin-echo IR method in terms of the SNR per unit time (59,64). Following the description of Look-Locker (LL) T_1-mapping presented by Chuang et al.(59), multiple time points are sampled during the relaxation following an inversion pulse separated by the interexcitation interval τ. This sampling is achieved using $N \times \mathrm{RF}$ pulses of the same flip angle (FA), α. Both Look and Locker (63) and Brix et. al (65) derive an expression for the signal evolution in the above LL T_1-mapping protocol. The partially relaxed longitudinal magnetization, $M(n)$, before each excitation pulse, can be described by an exponential recovery with time constant T_1^*.

$$M(n) = M(\infty) - \left[M(\infty) - M(0)\right]e^{-n\tau/T_1^*}, n = 0,1,\cdots,N-1 \ldots\ldots..(1)$$

where, $M(\infty) = M_{eq}\dfrac{1-e^{-\tau/T_1}}{1-e^{-\tau/T_1^*}}$. M_{eq} is the equilibrium longitudinal magnetization and the effective longitudinal relaxation time constant, T_1^* is related to the actual T_1, α and τ by;

$$\frac{1}{T_1^*} = \frac{1}{T_1} - \frac{\ln\cos(\alpha)}{\tau} \ldots\ldots(2)$$

The T_1 value for each pixel can be calculated by obtaining T_1^* from a three-parameter fit to equation 1, and substituting this into equation 2. However, this assumes that the exact FA is known for each pixel, which is a poor assumption. Due to inhomogineities in the B_1 field caused by imperfect excitation pulses and the RF coil profile, the FA differs from the intended value. This can be overcome by taking the relationship between $M(\infty)$ and $M(0)$, with T_1 being simplified to $T_1^* M(0)/M(\infty)$ when $\tau << T_1^*$, as shown by Steinhoff et. al (66). Chuang et al. (59) demonstrate how $M(\infty)/M(0)$, T_1^*, and therefore T_1, can be obtained independent of knowing the precise FA, and without the requirement that τ and T_d, the delay time between the inversion and the first excitation pulse of a slice, are short. This is achieved under the assumption that the longitudinal magnetization before each inversion pulse has reached steady state.

Such a Look Locker T_1-mapping MRI pulse sequence is applied in this study, with a total imaging time per T_1 map of approximately 43 minutes. The study aims to characterize the relationship between the infused $MnCl_2$ dose and the absolute tissue relaxation times, which could be used to optimize current manganese infusion protocols by minimizing the potential toxic effects of Mn^{2+} while still achieving adequate signal enhancement. By fitting this dose dependent data to *ex vivo* absolute Mn concentration values it could be possible to produce Mn concentration maps and to quantify the manganese content *in vivo*.

In order to obtain reliable relaxation rate data and accurate dose dependent calibrations the T_1 maps must be acquired at the appropriate time. The T_1-map sequence should not be initiated until after assumed blood pool washout, and acquisitions should be minimized during any periods of rapid temporal signal washout that may occur. Blood

pool washout has been estimated to occur over the order of approximately 15 minutes in a canine model (52). In this present study a temporal signal washout curve was produced from T_1 maps acquired at multiple time points post-infusion. The form of this curve could also provide information about the manganese efflux mechanisms.

One of the primary goals of this study is to characterize the efficacy of MEMRI T_1-mapping in assessing the dynamic features of calcium response due to myocardial injury in a small murine model. To achieve this Mn concentration map data was acquired for a myocardial infarction model allowing for estimates of the absolute Mn concentration both within the injury site and in the adjacent zone. The sensitivity of this technique could be used for potential pre-clinical and translational models to allow for treatment monitoring and for identifying potentially salvageable myocardium.

CHAPTER 2

MATERIALS AND METHODS

2.1 Animal Preparation

Manganese-enhanced MRI experiments were performed in adult male C57Bl/6 mice (5-13 weeks old, mean ± SD weight 22.6±2.2 g) following the guidelines of the Animal Care and Use Committee and the Animal Health and Care Section of the Institute (Medical College of Georgia, Augusta, GA, USA). The animals were initially anesthetized with a mixture of medical air, oxygen (1:1), and 2.5% isoflurane, positioned prone upon the animal cradle and maintained at 1.25±0.32% isoflurane throughout the MRI session. This protocol was established to maintain a relatively constant level of anesthesia and heart rate (460±30 bpm) during the MRI experiment. A custom made water bed was placed in the mouse cradle to maintain a constant temperature of 37.8 °C throughout imaging.

A tail vein line for manganese infusion was introduced after anesthesia. A 60 mM $MnCl_2$ solution was produced by dissolving $MnCl_2$ crystals in saline. For the dose dependent study, $MnCl_2$ was infused into control mice at doses ranging from 25 to 297 nmoles/g total body weight (BW). This dose range had previously been shown not to cause cardiac depressive effects (23). For the temporal washout study, a single dose of 282.57±5.96 nmoles/g BW was infused into the control mice. All infusions were completed at a constant rate of 0.6 ml/hr with the aid of a syringe pump (KD Scientific Inc., Holliston, MA, USA).

2.2 Myocardial Infarction Model

For the myocardial infarction study the mice were divided into three experimental groups: control (n = 6, 22.57±3.24 g), sham-operated (n = 21, 23.06±2.48 g) and myocardial infarction (MI) (n = 6, 23.24±1.02 g). The control group underwent no surgical procedures. The sham-operated and MI groups were anesthetized with an intraperitoneal ketamine/xylazine cocktail and placed in a supine position. A midline cervical incision was made to intubate the trachea. The intubated mice were connected to a rodent ventilator (CWE Inc., Ardmore, PA, USA) and were ventilated at a respiratory rate of 90 breaths per minute. The chest was opened by middle thoracotomy at upper sternum, between the fourth and fifth ribs. The sham-operated mice underwent open chest procedures without ligation of the left anterior descending (LAD) coronary artery. In the myocardial infarction studies, myocardial infarcts were produced by permanently ligating the LAD. The LAD was ligated at a position ~1 mm below the left auricle with an 8-0 polypropylene monofilament suture (Ethicon Inc., Somerville, NJ, USA). The mice were allowed to recover in a recovery chamber at 38 ºC, and then were rested prior to imaging sessions.

Imaging was performed 13±4 days and 12±6 days post-surgery for the MI and sham-operated groups, respectively. The date range for imaging the MI mice was chosen from survival data for mice that have undergone MI surgery, according to the previous experiences within the lab. At approximately 10-13 days post-surgery the survival curve for MI mice has been observed to reach a plateau, suggesting an ideal time to image.

From prior experience it was also determined that at shorter times post-infarction the heart is going through a remodeling process involving multiple inflammatory processes. The inflammatory cells (i.e. macrophages) are also known to uptake Mn^{2+} (45). Imaging at this early time point post-infarction has therefore been reserved for future studies. Conversely, at long times of approximately 30 days post-infarction the mice experience heart failure.

The aim of this study is to characterize the efficacy of MEMRI T_1-mapping for assessing alterations in calcium homeostasis. To accomplish this aim, cardiac images were acquired at two time points, pre- and post- myocardial infarction, in a small murine model. The post-MI time point was chosen to emphasize calcium alteration after MI, while avoiding the pathological complexity of heart failure at later times.

For $MnCl_2$ administration in the myocardial infarction study, a tail-vein infusion line was placed and all three groups of mice were infused with 282.50±4.00 nmoles/g BW $MnCl_2$ at a constant rate of 0.6 ml/hr.

2.3 MRI

Images were acquired on a 7.0-T 20-cm horizontal bore BioSpec MRI spectrometer (Bruker Instruments, Billerica, MA, USA) equipped with a micro imaging gradient insert (950 mT/m). Animal setup procedures followed those previously described (23). A standard Bruker volume coil (35 mm inner diameter, Bruker Instruments, Billerica, MA, USA) was used to transmit and receive at ^1H frequency (300 MHz). ECG and respiratory signals were monitored by a physiological monitoring

system (SA Instruments, INC., Stony Brook, NY) with the ECG signal used to gate the MRI Gradient Echo Flow Compensation (GEFC) pulse sequence (67). All images were gated to be acquired directly after the ECG R-wave at end-diastole. For the MI group accurate gating was achieved due to regular ECG signals in our imaging timeframe post-infarction. The ECG signal is expected to become more problematic at longer times as the MI progresses. Breathing artifacts were minimized by securing the mouse in a custom made mouse holder.

Short axis images were acquired for the control and sham-operated mice midway through the left ventricle and perpendicular to the long axis of the heart. In the myocardial infarction group the short axis was again defined perpendicular to the long axis of the heart, but located at the area with the greatest LV wall-thinning due to the injury. This was typically within 1 mm of the center of the ventricle. The imaging parameters were as follows: matrix = 128 x 128; TE = 3.5 ms; TR = 35 ms; slice thickness = 1.0 mm; FOV = 3.0 x 3.0 cm; flip angle = 60° and six averages. The repetition time, TR, for the gradient echo sequence was purposely set at a time shorter than the RR period (130±2 ms). The true repetition time for the imaging sequence was therefore the RR period.

Both pre-$MnCl_2$ and post-$MnCl_2$ T_1 maps were acquired with a ECG-gated, flow-compensated Look-Locker MRI pulse sequence (matrix = 128 x 128; TE/TR = 2.5 ms/10 sec; slice thickness = 1.0 mm; FOV = 3.0 x 3.0 cm; NA = 2; inversion time = 9 ms; average echo interval = 130 ms; number of echo images = 50; flip angle = 10°) as previously described (59). The echo interval was set as the approximate mean RR period observed prior to the execution of each T_1 map sequence. The initial echo per repetition

was gated, with the subsequent echo pulses separated by the constant echo interval. The T_1 value estimations are therefore not affected by any RR period fluctuations that may occur during TR. Post-infusion T_1 maps were acquired approximately 5 mins after completion of the infusion to allow for assumed Mn^{2+} blood pool clearance. The total imaging time per T_1 map was approximately 43 minutes. T_1 maps were acquired both pre-$MnCl_2$ infusion and post-$MnCl_2$ infusion to allow the calculations of change in T_1 relaxation rate, ΔR_1, due to the infusion.

2.4 Analytical Procedures

Control mice were sacrificed immediately after imaging. Absolute manganese content for heart and blood samples were measured by inductively coupled plasma-mass spectrometry (ICP-MS) analysis (CANTEST Ltd., North Vancouver, BC, Canada).

2.5 Data Analysis

T_1-mapping

The T_1 value of each pixel was calculated using a custom-written C^{++} program (59). The signal recovery of each pixel was fitted from the 50 echo images by the three-parameter Levenburg-Marquardt non-linear curve-fitting algorithm. Region-of-interest (ROI) analysis was performed on the 2D T_1 maps using AMIDE (68) to calculate the average regional T_1 value. In the case of the control and sham-operated mice, ROI tools were used to select a region of interest within the left ventricular free wall (LV Wall). To

quantitatively assess the dynamic features of the calcium response due to the myocardial injury additional regions of interest were defined for the MI group. The adjacent zone ROIs were defined in the regions of the LV Wall immediately surrounding the injury site, starting at the outer boundary of the left ventricular thinning and extending approximately 1.5 mm into the viable tissue. An additional ROI, the myocardial infarction ROI (MI), was created within the injury site of the left ventricular free wall. *In vivo* ΔR_1 values were calculated as (post-$MnCl_2$ infusion R_1) – (pre-$MnCl_2$ infusion R_1), where the relaxation rate, R_1, is defined as $1/T_1$. ΔR_1 values are quoted as a mean ± standard deviation, in units of (1/sec).

Knowing the $MnCl_2$ infusion dose, the *ex vivo* absolute manganese values were correlated to the *in vivo* ΔR_1 values, allowing for an estimate of the absolute Mn content in the heart. From this information *in vivo* absolute Mn concentration maps were produced based on a relationship between R_1 values in the LV Wall and interventricular septum post-infusion, and the absolute Mn elemental analysis results.

Statistics

The differences in manganese induced relaxivity changes between the three animal groups in the myocardial infarction study were assessed using ANOVA with a Bonferroni correction test between sub-groups. The threshold for significance was set at $\alpha = 0.05$. Differences between individual groups were assessed using a two-tailed t-test, with the significance threshold set at $p < 0.05$.

CHAPTER 3

RESULTS

Sample ECG gated short-axis cardiac MRI images for a control mouse are shown in Figure 1. Figures 1a and b show the T_1-weighted signal intensity enhancements pre- and post-$MnCl_2$ infusion, respectively. Figures 1c and d show the corresponding T_1 maps pre- and post-$MnCl_2$ infusion, respectively. At this $MnCl_2$ dose of 280 nmoles/g BW there is significant signal intensity enhancement in the myocardium following $MnCl_2$ infusion. For the control mice, a region of interest (ROI) was created for the left ventricular free wall (LVWall), Figure 1b. T_1 values were obtained from both pre-$MnCl_2$ infusion T_1 map ROIs and post-$MnCl_2$ infusion T_1 map ROIs and ΔR_1 was calculated as the difference between these two T_1 values ($\Delta R_1 = \Delta(1/T_1)$).

3.1 Concentration Dependent Study

In order to produce *in vivo* Mn concentration maps, two pieces of information are required. One is the dependence of manganese infusion dose on LV Wall relaxivity, and the other is the absolute tissue Mn concentration following manganese infusion. The effect of altering the infusion dose on LV Wall ΔR_1 is shown Figure 2, with the data summarized in Table 1. The post-$MnCl_2$ infusion T_1 map sequence was initiated approximately 5 minutes post-infusion. The summarized T_1 map data points are shown as triangles in Figure 2, with the sample size and uncertainty (±1 SD) shown. The first two

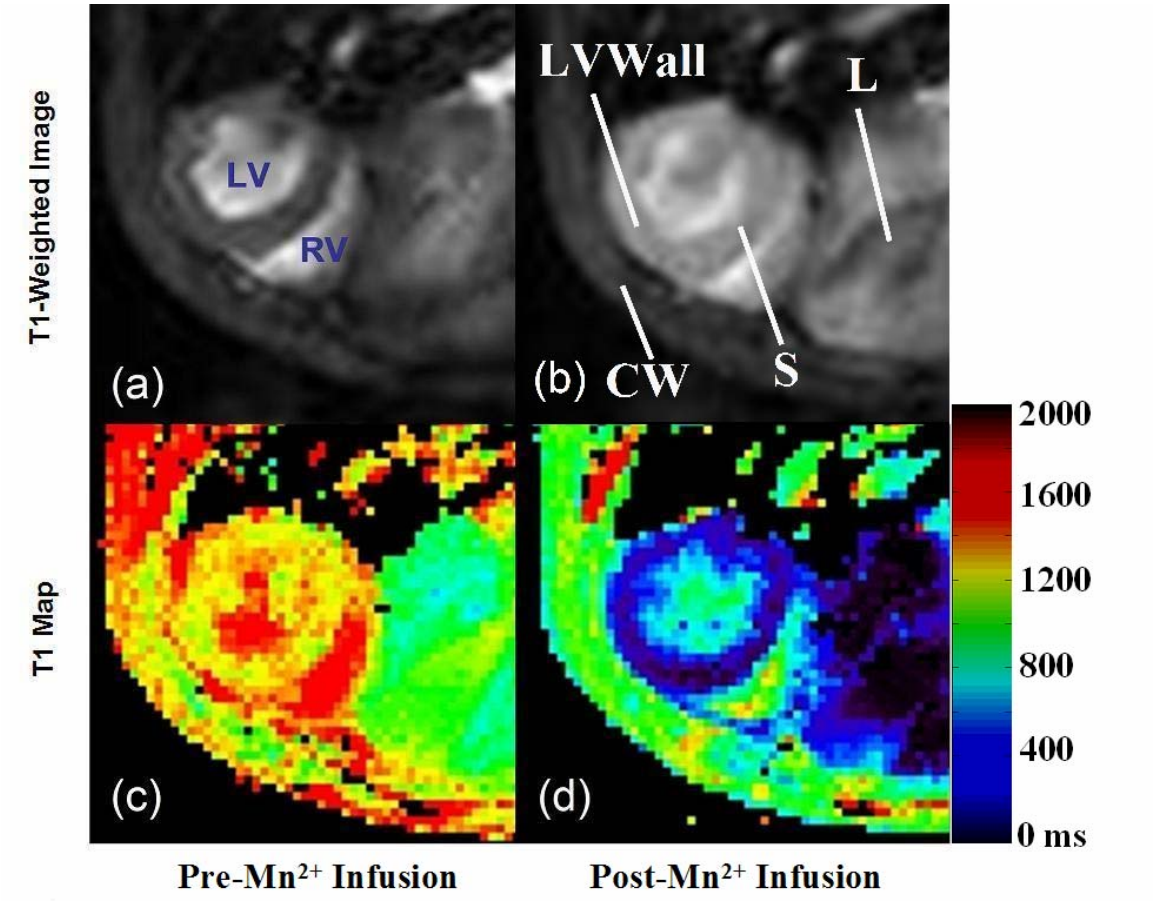

Figure 1 - Example short-axis heart images for a control mouse. (a) T_1-weighted pre-$MnCl_2$ infusion image; (b)T_1-weighted post-$MnCl_2$ infusion image; (c) pre-$MnCl_2$ infusion T_1 map; (d) post-$MnCl_2$ infusion T_1 map. (b) shows the locations of the interventricular septum (S), left ventricular free wall (LVWall), liver (L) and chest wall (CW)

columns in Table 1 display the grouped $MnCl_2$ infusion doses and corresponding LV Wall ΔR_1. The sample sizes are displayed in parentheses. ΔR_1 values ranged from 0.16 /sec for the lowest dose regime, up to an average of 4.61 /sec for doses above 197 nmoles/g BW

Also shown in Figure 2 and Table 1 are the elemental analysis results for the heart tissue and blood sample absolute manganese concentrations. Absolute manganese

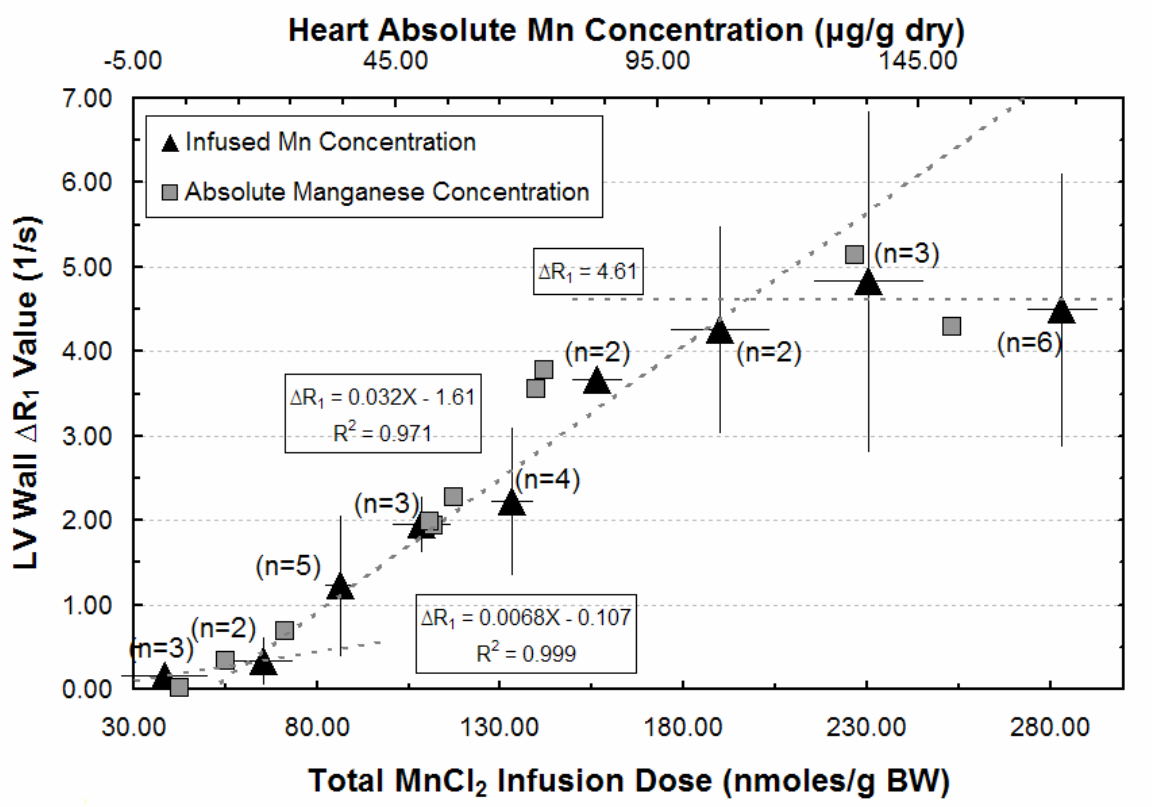

Figure 2 - Effect of altering the dose of infused $MnCl_2$ on left ventricular free wall relaxivity (triangles). The x-axis shows the total dose of infused $MnCl_2$ normalized to mouse BW. The y-axis shows the relaxivity change, ΔR_1, pre- vs. post-$MnCl_2$ infusion. As a function of dose, two linear dose uptake regions were noted, along with a plateau region above 197 nmoles/g BW. The least square fits are shown with total $MnCl_2$ infusion dose, X, in nmoles/g BW. Comparison of this data to the total heart manganese concentration (µg/g dry) as determined by ICP-MS (squares) is also shown. This plot can be used to estimate the Mn concentration *in vivo*

concentration values were quantified using ICP-MS, and are shown in columns 3-5 of Table 1.

Three regions can be fit to Figure 2. At $MnCl_2$ infusion doses, X (nmoles/g BW), below 197 nmoles/g BW two linear uptake regimes can potentially be fit to the data, intercepting at 61 nmoles/g BW. Above 197 nmoles/g BW, the relaxivity enhancement reaches a plateau. Within this physiological steady state any further increase in $MnCl_2$

Table 1 - Dose dependent T_1 map ΔR_1 values for the LV Wall are shown in columns 1 and 2. ICP-MS absolute blood and heart manganese values from mouse samples are displayed in columns 3-5. LV Wall ROI absolute Mn concentrations from the calculated concentration maps are given in the final column.

$MnCl_2$ Infusion Dose (nmoles/g BW)	**LV Wall ΔR_1 (1/sec)**	**$MnCl_2$ Infusion Dose for Elemental Analysis (nmoles/g BW)**	**Heart Absolute Mn Concentration (µg/g dry weight)**	**Blood Absolute Mn Concentration (µg/ml)**	**Concentration Map LV Wall ROI Data (nmoles/g)**
38.34±11.98 (n=3)	0.16±0.17	37.55±16.82 (n=2)	8.15±6.04	0.22±0.04	6.48±7.78
65.46±8.16 (n=2)	0.33±0.29	-	-	-	12.22±8.87
86.21±4.37 (n=5)	1.23±0.84	83.85	23.78	0.41	36.05±23.91
108.33±8.09 (n=3)	1.96±0.34	108.87±11.36 (n=2)	53.87±3.31	0.41±0.03	63.16±10.65
132.98±5.92 (n=4)	2.23±0.87	130.38	52.32	0.53	80.04±35.68
156.17±7.01 (n=2)	3.67±0.15	156.17±7.01 (n=2)	72.72±1.03	0.55±0.09	114.52±13.04
189.89±13.59 (n=2)	4.26±1.24	199.50	132.74	0.61	139.74±77.11
230.40±15.10 (n=3)	4.83±2.02	243.17	151.35	0.69	166.41±77.11
283.13±9.73 (n=6)	4.49±1.63	-	-		221.97±131.13

Values are expressed as mean ± SD, with sample size in parentheses

dose does not result in any apparent increase of ΔR_1. The plateau occurs at ΔR_1 = 4.61±1.64 /sec. The best fit for the two phases below 197 nmoles/g BW have the form $\Delta R_{1,low} = 0.007X - 0.107$ (r^2 = 0.999) and $\Delta R_{1,high} = 0.032X - 1.613$ (r^2 = 0.971) for the doses below and above 61 nmoles/g BW, respectively. This biphasic fit is consistent with findings from data from our lab taken in a rat model. The lower curve is fit under the assumption that $\Delta R_1 = 0$ below 16.3 nmoles/g BW. This is deduced visually from Figure 2 and is consistent with the fact that there is initially a non-zero volume of saline infused prior to Mn^{2+} entering the mice, inherent in the infusion line setup. For the average mouse weight of 22.6±2.2 g, the average dose of saline present in the infusion line is 16.3±0.7 nmoles/g. The correlation between the infused $MnCl_2$ dose, X (nmoles/g BW), and absolute heart Mn concentration, Y (μg/g dry weight), can be fit linearly with $Y = 0.70X - 25.9$ (r^2 = 0.94, Figure 3a). Similarly, the effect of altering the dose of infused $MnCl_2$ on absolute blood sample manganese concentration, Z (μg/ml), yields a linear relationship of $Z = 0.002X + 0.16$ (r^2 = 0.93, Figure 3b).

One of the primary goals for this study is to quantitatively estimate the absolute manganese map for the heart, *in vivo*. The data presented in Figure 2 shows the relationship between ΔR_1 and the absolute heart manganese concentration, where the elemental analysis data points (square data point) are overlaid onto the dose dependent plot (triangular data points). Using the data obtained from this dose dependent study a myocardial relaxivity of 5.17 $mM^{-1}s^{-1}$ was estimated, based on the measured R_1 values in the myocardium and from the elemental analysis measurements. Using this relaxivity, *in vivo* absolute Mn concentration maps (nmoles/g) were produced. The LV Wall ROI data for these maps are shown in the final column of Table 1.

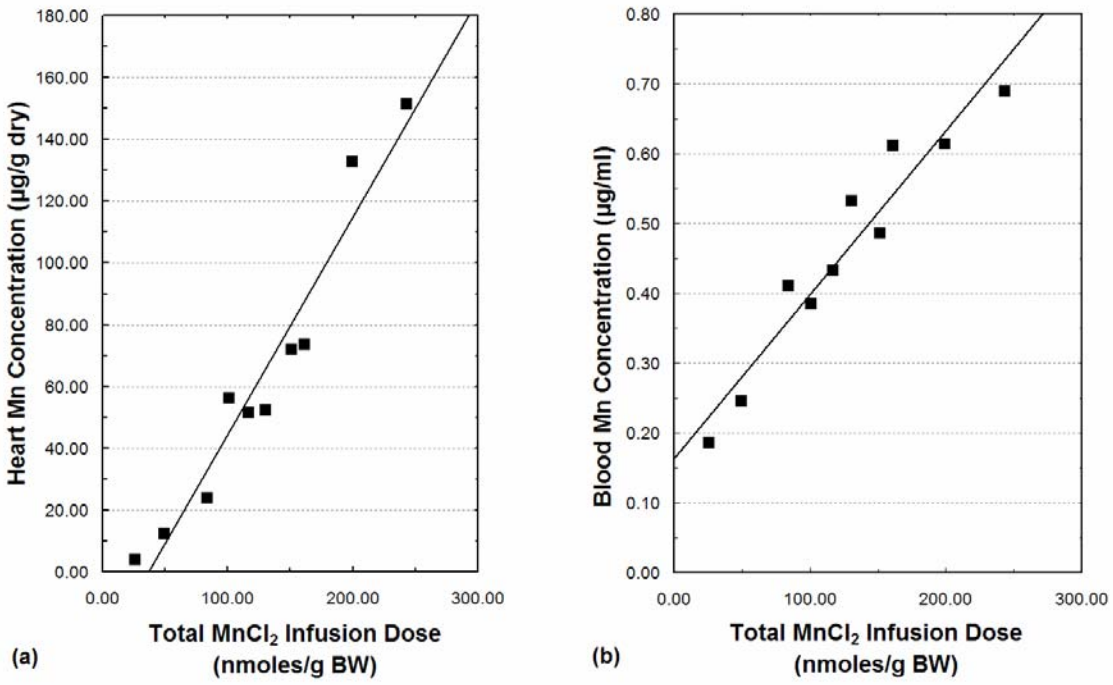

Figure 3 - Effect of $MnCl_2$ infusion dose on the total manganese concentration determined by ICP-MS for (a) the heart and (b) blood. The x-axis shows the total dose of $MnCl_2$ infused. The y-axis shows the absolute manganese concentration in µg/g dry weight for the heart and µg/ml for the blood. Both plots show the linear least square best fit to the data

3.2 Temporal Washout Study

The feasibility of using the T_1-mapping technique was also applied to study the manganese washout phenomena temporally. This is important because it will provide us with a quantitative means of measuring the rate of manganese efflux from the myocardium, and could also potentially provide information into individual compartment efflux rates. The temporal characteristics of ΔR_1 post-$MnCl_2$ infusion were studied in control mice infused at a single dose of 282.57±5.96 nmoles/g BW $MnCl_2$. The washout period was examined from 0.2 – 99.2 hrs. Values of ΔR_1 were calculated by subtracting

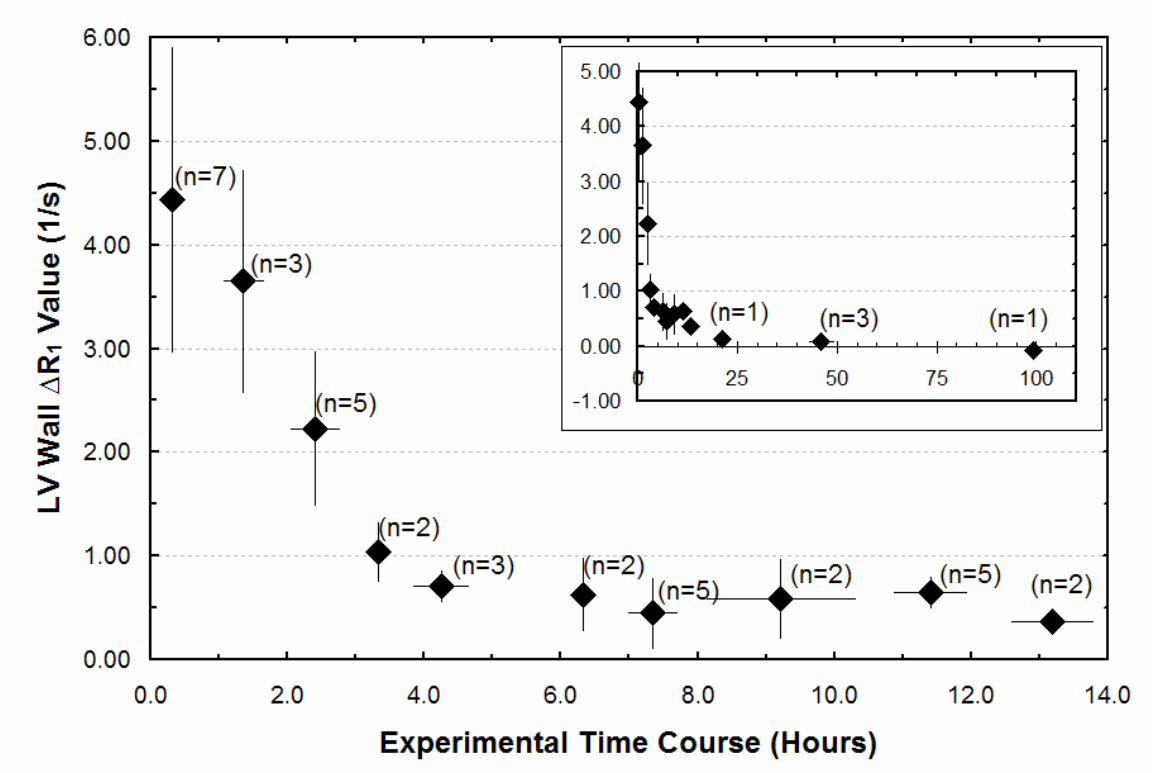

Figure 4 - Temporal Mn^{2+} washout curve. The x-axis shows experimental time course post-$MnCl_2$ infusion, in hours. The y-axis shows the difference in relaxation rate, ΔR_1, pre- vs. post-$MnCl_2$ infusion. The insert plot shows the complete washout curve over an extended period of time

the average baseline ROI R_1 ($R_{1,baseline,LVWall} = 0.78 \pm 0.04$ /sec, from 33 control mice) from the post-$MnCl_2$ infusion ROI R_1 value. Figure 4 shows the temporal relationship of the Mn^{2+} washout curve in the LV Wall, while Table 2 summarizes the washout data for the LV Wall. The LV Wall ΔR_1 signal has attenuated 50% in the first 2.5 hours post-infusion.

Despite this initially rapid attenuation of the ΔR_1 signal, there is a non-zero ΔR_1 value remaining until a few days post-infusion suggesting retention of the remaining Mn^{2+}. During the first 9 hours post-infusion the washout data for this infusion dose can be fit exponentially with LV Wall $\Delta R_1 = (5.24 \text{ /sec}) e^{-0.40 \cdot t}$ ($r^2 = 0.93$, with t given in units

Table 2 - Temporal ΔR_1 signal attenuation post-$MnCl_2$ infusion in the LV Wall.

Time Post-$MnCl_2$ Infusion (hrs)	**LV Wall ΔR_1 (1/sec)**
0.31±0.11 (n=7)	4.44±1.48
1.35±0.30 (n=3)	3.65±1.08
2.41±0.37 (n=5)	2.23±0.75
3.33±0.04 (n=2)	1.04±0.29
4.25±0.41 (n=3)	0.70±0.16
6.33±0.08 (n=2)	0.63±0.36
7.34±0.37 (n=5)	0.45±0.35
9.22±1.11 (n=2)	0.59±0.39
11.40±0.54 (n=5)	0.64±0.16
13.19±0.62 (n=2)	0.36±0.03
21.11 (n=1)	0.14
46.07±3.30 (n=3)	0.07±0.04
99.19 (n=1)	0.08

Values are expressed as mean ± SD, with sample size in parentheses

of hours). At longer times further data is required to produce an exponential fit to assess potential compartmentalization. This information provides a better imaging timeframe for the cardiovascular disease model in the current study, with eventual information on potential extrudability of Mn^{2+} from the myocardium.

3.3 Myocardial Infarction Study

The final part of this study involved utilizing the T_1-mapping method under cardiovascular disease conditions to examine the feasibility of applying such a technique. *In vivo* concentration map calculations were performed on a mouse myocardial infarction model to investigate the ability of quantitatively assessing dynamic changes in manganese uptake in various regions of myocardial injury. All three groups of mice, namely control, sham-operated and myocardial infarction, were infused with a single dose of 282.50±4.00 nmoles/g BW $MnCl_2$. The mice were imaged at 0.25±0.05 hrs after the initial $MnCl_2$ infusion, as indicated from the temporal washout study to avoid modulated Mn^{2+} retention. Figure 5 shows sample post-$MnCl_2$ infusion T_1 maps for (a) sham-operated and (b) myocardial infarction mice. The sham-operated mouse shows a well defined LV Wall and interventricular septum with relatively uniform manganese uptake throughout. In the MI model there is substantial LV Wall thinning at the injury site, accompanied by higher T_1 values due to reduced uptake of Mn^{2+}.

The results of this study are shown in Figure 6, where the data is presented as the average ROI ΔR_1 (solid horizontal line) ± SD (shaded box), with the data range (solid vertical line). Table 3 also shows these results, along with the statistical test results. The relatively large sample size for the sham-operated group resulted from the time required to optimize the surgical technique, in preparation for consistent MI production. Twenty-one sham-operated surgeries were performed to ensure consistency in the technique before performing MI surgery. Imaging results for all of the sham operations were self-consistent (i.e., there is no image-based trend between the time of surgery and the value of LV Wall ΔR_1).

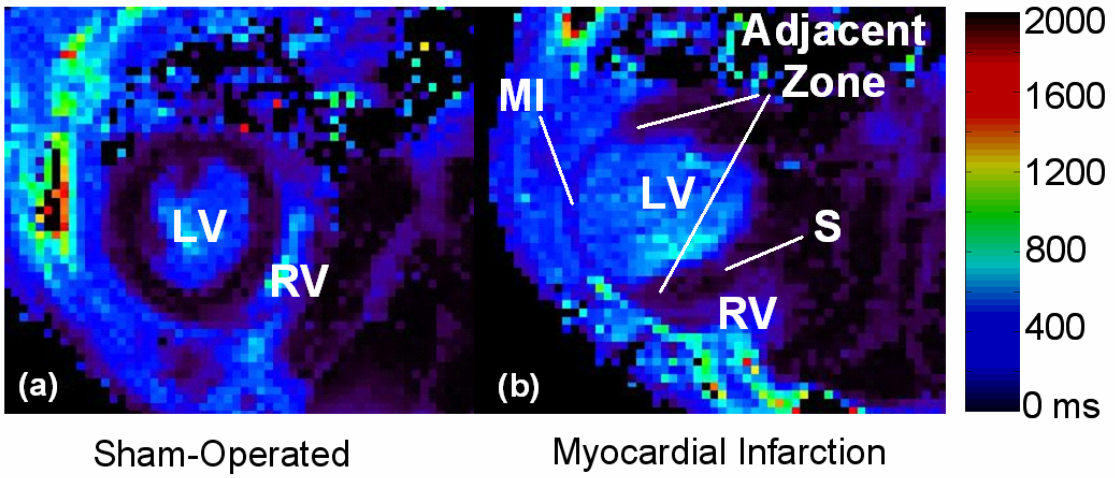

Figure 5 - Example short-axis post-$MnCl_2$ infusion T_1 map cardiac images for; (a) a sham-operated mouse, and (b) a myocardial infarction mouse. Significant LV Wall thinning can be seen for the MI mouse with longer T_1 relaxation times relative to healthy myocardial tissue. (b) shows the interventricular septum (S), myocardial infarction adjacent zone (Adjacent Zone) and myocardial infarction injury site (MI)

There is no statistically significant difference between the LV Wall ΔR_1 values of the control (4.49±1.63 /sec) and sham-operated (4.62±2.34 /sec) mice ($p = 0.91$) suggesting that the procedure of opening the chest does not affect Mn^{2+} uptake within the heart. Comparing the control and sham-operated LV Wall ΔR_1 values with the MI adjacent zone ΔR_1 values using ANOVA, however, shows that there is a significant difference in relaxivity between the groups ($p = 0.03$). Cross-comparison of all of the groups individually with t-tests demonstrates that the MI adjacent zone ΔR_1 (2.00±0.49 /sec) is significantly less than the control and sham-operated groups ($p < 0.05$), with the MI injury site ΔR_1 (0.97±0.39 /sec) being significantly less ($p < 0.05$) than all of the groups. These results demonstrate the sensitivity of this technique to determine altered manganese uptake, not only at the necrotic site but also within the adjacent zone. Calculating the *in vivo* Mn concentration map could allow for potentially salvageable

myocardium to be identified for future therapeutic treatment or prevention, in preclinical models.

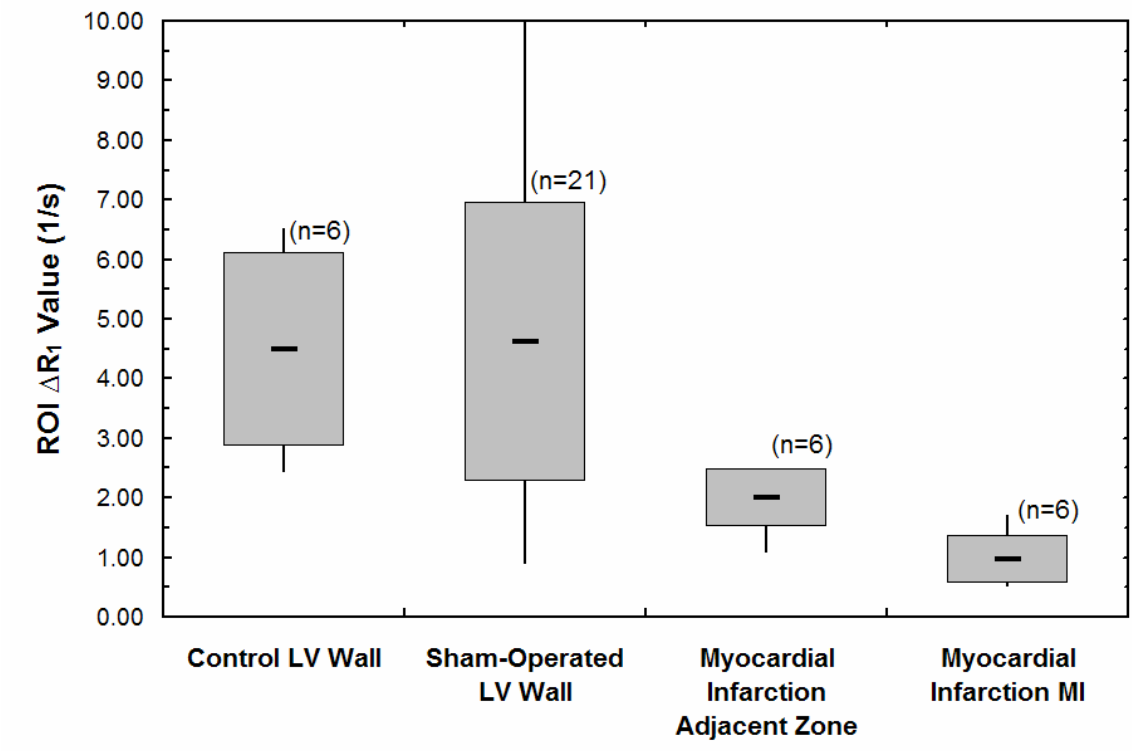

Figure 6 - The effect of myocardial injury on the uptake of Mn^{2+}. Regions of interest were defined for the LV Wall in the control and sham-operated groups. ROIs for the MI model were also defined at the injury site contained within the LV Wall and in the myocardial infarction adjacent zone, immediately surrounding the injury site. Data is presented as the average ROI ΔR_1 (solid horizontal line, /sec) ± SD (shaded box), with the data range shown (solid vertical line).

Table 3 - Average ΔR_1 signal enhancement post-$MnCl_2$ infusion for control, sham-operated and myocardial infarction groups. For the myocardial infarction group ROIs were defined both for the myocardial infarction adjacent zone, surrounding the infarction site, and the infarcted site (MI).

Group - Region of Interest (ROI)	**ROI ΔR_1 (1/sec)**
Control – LV Wall	4.49±1.63 (n=6)$^{\dagger *\ddagger}$
Sham-Operated – LV Wall	4.62±2.34 (n=21)
Myocardial Infarction – Adjacent Zone	2.00±0.49 (n=6)
Myocardial Infarction – MI Site	0.97±0.39 (n=6)

Values are expressed as mean ± SD, with sample size in parentheses
$^{\dagger}p = 0.03$ between all LV Wall groups (ANOVA, single factor)
$^{*}p = 0.91$ between control and sham-operated LV Wall groups (unpaired two-tailed t-test)
$^{\ddagger}p < 0.05$ between every two group combination except the control and sham-operated LV Wall combination (unpaired two-tailed t-test)

CHAPTER 4

DISCUSSION

It has previously been shown (51) that T_1-weighted MEMRI in a murine MI model provides clear delineation of the myocardial infarction site. The present study has demonstrated the quantitative ability of MEMRI T_1-mapping in the murine heart to determine cellular viability in the vicinity of the myocardial infarction site. This could ultimately lead to an early *in vivo* indicator of viable treatment options depending on the state of the myocytes and their potential salvageability.

T_1-mapping of cardiac MEMRI has demonstrated enough sensitivity to provide quantitative information over the range of $MnCl_2$ doses used in our experiment. By demonstrating the dynamic range of relaxivity changes over a range of $MnCl_2$ infusion doses this method can provide a means of optimizing $MnCl_2$ infusion protocols. Mn^{2+} is know to be cardiotoxic at high doses (55). However, we have demonstrated a large range of signal enhancement at subtoxic levels. Due to this fact, lower doses of $MnCl_2$ can be used while still producing significant relaxivity changes.

Results of the dose dependent study (Figure 2) not only allow for the design of contrast agent optimal doses to minimize toxicity concerns, but also allow *in vivo* estimates of absolute Mn concentration following LV Wall ΔR_1 calculations. This technique can therefore be used to monitor the *in vivo* Mn levels non-invasively. One interesting observation is the non-linear relationship between the total $MnCl_2$ infusion dose and the LV Wall ΔR_1. Instead of a purely linear increase in signal intensity enhancement a plateau region occurs at a dose above 197 nmoles/g BW, likely due to

physiological effects. This is in good agreement with previously reported results (23). Following the same non-linear form as the total infusion dose, it is seen that above approximately 100 μg/g dry heart weight, the absolute Mn concentration also reaches a plateau. Within this plateau there is no increase in ΔR_1 following an increase in absolute heart manganese concentration. As the infusion of $MnCl_2$ increases, the absolute Mn content of the heart also increases (Figure 3a), but ΔR_1 reaches a plateau at 4.61 /sec.

The plateau effect can be potentially explained in a number of ways, either due to the limitations of Ca^{2+} uptake, or due to limited compartmentalization. The cellular binding sites could become saturated at a certain dose, limiting the uptake of Mn^{2+}. Another explanation for the plateau phenomena could be due to a gradient effect whereby the cells become saturated and are unable to uptake more Mn^{2+}. Similarly, Mn^{2+} could have an inhibitory effect on the Ca^{2+} channels, limiting the scope for Mn^{2+} uptake. Further observations are necessary to decipher the physiology of this phenomenon.

The non-zero intercept in Figure 2 is in part due to the finite length of infusion tubing attached to the tail vein needle. A short, 9.9±0.4 cm, length of PE10 tubing containing saline solution connects the infusion needle to the $MnCl_2$ infusion line. This length of tubing corresponds to an equivalent infusion dose of 16.3±0.7 nmoles/g BW $MnCl_2$. This helps to validate our assumption for the low dose linear fit, where at doses below 16.3 nmoles/g BW there is assumed to be no manganese infusion and $\Delta R_1 = 0$.

Despite the number of applications of Mn^{2+} as an MRI contrast agent, little detail is known about the efflux mechanisms of Mn^{2+} from myocytes. The signal washout from the LV Wall is shown in Figure 4. After 2.5 hours 50% of the ΔR_1 signal had been attenuated in the LV Wall, with a small non-zero ΔR_1 remaining until a few days post-

infusion. In comparison, it has been shown in a rat model that manganese is cleared from all the major organs within 24 hours (69).

The form of this washout curve is still uncertain; numerical modeling of Mn transport may provide additional insight. The complicated form of this curve could contain information about the Mn^{2+} efflux mechanisms within the myocardium. Accumulation of Mn^{2+} in various compartments within the myocytes could explain the variations between the initially rapid washout and the sustained signal enhancement over a few days. Differences in individual compartment efflux rates would contribute to the washout curve. One potential efflux mechanism is via the sodium-calcium exchanger (NCX). The NCX is an important transporter for the regulation of intracellular Ca^{2+} concentration (70). By altering the characteristics of different efflux mechanisms, such as the NCX channel, it might be possible to further interrogate the form of the curve and the underlying physiology. This information, along with the use of physiological modulators such as pharmaceutical agents, could be critical for examining potential Mn^{2+} extrudability pathways. This technique could also provide a means of identifying Mn^{2+} efflux modulation due to myocardial injury.

The myocardial infarction study utilized the optimal dose and timing properties acquired from the previous sections of this study. We are able to show statistically significant differences between healthy myocardial tissue, in the control and sham-operated groups, and the MI adjacent zone in the MI group. Mn^{2+} had previously been shown to provide functional, pathological and viability data in myocardial tissue using T_1-weighted imaging techniques in mice (51) and dogs (52). Manganese-dipyridoxyl diphosphate (MnDPDP), a Mn^{2+} releasing contrast agent (71), is currently approved for

clinical liver imaging. MnDPDP-enhanced images have demonstrated manganese retention in viable pig myocardium (72) with clearance of manganese from infarcted myocytes in a rat model (50). This behavior is consistent with MEMRI contrast. Recently, MnDPDP has been used as a viability marker in patients with myocardial infarction (47). However, more quantitative information was required to be able to assess the extent of damage to the myocardium, which we have demonstrated through the T_1-mapping protocol.

Myocardial infarction causes physiological remodeling leading to potential Ca^{2+} handling alterations. This remodeling process can potentially be observed and monitored using manganese enhanced T_1-mapping as shown by the sensitivity of our data. The injury site of the LV Wall showed a ΔR_1 almost 5 times less than the healthy LV Wall of the control mouse. More interestingly, with respect to recovery of the injured tissue, this technique is sensitive to the reduced uptake of Mn^{2+} in the adjacent zone. During myocardial ischemia intracellular calcium concentrations increase due to increased Ca^{2+} influx and reduced efflux (9). However, our results show reduced Mn^{2+} uptake in both the MI site and adjacent zone.

The phenomena of reduced Mn^{2+} uptake in both the MI region and the adjacent zone are complex to address. To date conflicting results have been reported in other studies. *In vivo* manganese enhanced MRI has observed signal attenuations in mice (51), rat (73) and larger mammalian species (74). However, *in vitro* studies have shown enhanced Ca^{2+} influx as a way of a compensatory process (75).

Camellitti, et al. (76) have shown *ex vivo* results which demonstrate small islands of viable myocytes in ischemic regions. These islands could potentially explain the non-

zero Mn^{2+} uptake in the ischemic regions. In the adjacent area we suggest that the volume of viable tissue is still reduced as compared to healthy LV Wall tissue of the control and sham operated mice. This could potentially explain the reduction of Mn^{2+} uptake in this area. Temporal responses to myocardial infarction could now be predicted in mice using this preclinical model, looking at the alterations in calcium handling with recovery.

CHAPTER 5

CONCLUSIONS

This study demonstrates that T_1-mapping of cardiac manganese-enhanced MRI can be used to quantify *in vivo* Mn concentrations and define regions of potentially altered Ca^{2+} homeostasis in a myocardial infarction model. The effect of manganese infusion dose has been studied up to approximately 297 nmoles/g BW, with an initial slow uptake occurring below 61 nmoles/g BW, and a more rapid uptake until 197 nmoles/g BW. At this dose the physiological steady state was achieved.

Mn^{2+} washout has also been investigated in the LV Wall. The ΔR_1 signal is attenuated to 50% of the steady state signal in approximately 2.5 hours post-infusion. There is still a ΔR_1 effect remaining after a few days suggesting potential Mn^{2+} retention at the site. The overall washout progression warrants further investigation, but this technique could provide a potential way to examine the extrudability of Mn^{2+} from the myocardium.

One motivation for this study is that myocardial infarction causes physiological remodeling leading to potential Ca^{2+} handling alteration. With the potential of using T_1-mapping and ICP-MS analysis to quantify the *in vivo* concentration of Mn, more insight into myocardial infarction adjacent zones may be provided. This technique could provide additional information such as: (1) optimization of the $MnCl_2$ dose to minimize the study dose; (2) quantification of Mn concentration *in vivo*; (3) temporal response of myocardial infarction or ischemic-reperfusion model(s); (4) pharmacological efficacy; and (5) potential preclinical and translational models to monitor disease treatment.

REFERENCES

1. Dhalla NS, Pierce GN, Panagia V, Singal PK, Beamish RE. Calcium movements in relation to heart function. *Basic research in cardiology* 1982; **77**; 2: 117-139.

2. Wier WG. Intracellular calcium during excitation-contraction coupling in mammalian ventricle. *Medicine and science in sports and exercise* 1991; **23**; 10: 1149-1156.

3. Mukherjee R, Spinale FG. L-type calcium channel abundance and function with cardiac hypertrophy and failure: a review. *Journal of molecular and cellular cardiology* 1998; **30**; 10: 1899-1916.

4. Eisner DA, Sipido KR. Sodium calcium exchange in the heart: necessity or luxury? *Circulation research* 2004; **95**; 6: 549-551.

5. Caroni P, Carafoli E. An ATP-dependent Ca^{2+}-pumping system in dog heart sarcolemma. *Nature* 1980; **283**; 5749: 765-767.

6. Houser SR, Piacentino V, 3rd, Weisser J. Abnormalities of calcium cycling in the hypertrophied and failing heart. *Journal of molecular and cellular cardiology* 2000; **32**; 9: 1595-1607.

7. Saini HK, Shao Q, Musat S, Takeda N, Tappia PS, Dhalla NS. Imidapril treatment improves the attenuated inotropic and intracellular calcium responses to ATP in heart failure due to myocardial infarction. *British journal of pharmacology* 2005; **144**; 2: 202-211.

8. Zhang XQ, Musch TI, Zelis R, Cheung JY. Effects of impaired Ca^{2+} homeostasis on contraction in postinfarction myocytes. *J Appl Physiol* 1999; **86**; 3: 943-950.

9. Menown IB, Adgey AA. Cardioprotective therapy and sodium-hydrogen exchange inhibition: current concepts and future goals. *Journal of the American College of Cardiology* 2001; **38**; 6: 1651-1653.

10. Orrenius S, Zhivotovsky B, Nicotera P. Regulation of cell death: the calcium-apoptosis link. *Nature reviews* 2003; **4**; 7: 552-565.

11. Sam F, Sawyer DB, Chang DL, Eberli FR, Ngoy S, Jain M, Amin J, Apstein CS, Colucci WS. Progressive left ventricular remodeling and apoptosis late after myocardial infarction in mouse heart. *American journal of physiology* 2000; **279**; 1: H422-428.

12. Lerman A, Zeiher AM. Endothelial function: cardiac events. *Circulation* 2005; **111**; 3: 363-368.

13. Jain AP, Mohan A, Gupta OP, Jajoo UN, Kalantri SP, Srivastava LM. Role of oxygen free radicals in causing endothelial damage in acute myocardial infarction. *The Journal of the Association of Physicians of India* 2000; **48**; 5: 478-480.

14. van Dokkum RP, Eijkelkamp WB, Kluppel AC, Henning RH, van Goor H, Citgez M, Windt WA, van Veldhuisen DJ, de Graeff PA, de Zeeuw D. Myocardial infarction enhances progressive renal damage in an experimental model for cardio-renal interaction. *J Am Soc Nephrol* 2004; **15**; 12: 3103-3110.

15. Roy D, Quiles J, Sinha M, Aldama G, Gaze D, Kaski JC. Effect of direct-current cardioversion on ischemia-modified albumin levels in patients with atrial fibrillation. *The American journal of cardiology* 2004; **93**; 3: 366-368.

16. Tsutsui H, Ide T, Hayashidani S, Suematsu N, Shiomi T, Wen J, Nakamura K, Ichikawa K, Utsumi H, Takeshita A. Enhanced generation of reactive oxygen species in the limb skeletal muscles from a murine infarct model of heart failure. *Circulation* 2001; **104**; 2: 134-136.

17. Lindley TE, Doobay MF, Sharma RV, Davisson RL. Superoxide is involved in the central nervous system activation and sympathoexcitation of myocardial infarction-induced heart failure. *Circulation research* 2004; **94**; 3: 402-409.

18. Mendonca-Dias MH, Gaggelli E, Lauterbur PC. Paramagnetic contrast agents in nuclear magnetic resonance medical imaging. *Seminars in nuclear medicine* 1983; **13**; 4: 364-376.

19. Cory DA, Schwartzentruber DJ, Mock BH. Ingested manganese chloride as a contrast agent for magnetic resonance imaging. *Magnetic resonance imaging* 1987; **5**; 1: 65-70.

20. Anderson M. Mn ions pass through calcium channels. A possible explanation. *The Journal of general physiology* 1983; **81**; 6: 805-827.

21. Narita K, Kawasaki F, Kita H. Mn and Mg influxes through Ca channels of motor nerve terminals are prevented by verapamil in frogs. *Brain research* 1990; **510**; 2: 289-295.

22. Shibuya I, Douglas WW. Indications from Mn-quenching of Fura-2 fluorescence in melanotrophs that dopamine and baclofen close Ca channels that are spontaneously open but not those opened by high $[K^+]O$; and that Cd preferentially blocks the latter. *Cell calcium* 1993; **14**; 1: 33-44.

23. Hu TC, Pautler RG, MacGowan GA, Koretsky AP. Manganese-enhanced MRI of mouse heart during changes in inotropy. *Magn Reson Med* 2001; **46**; 5: 884-890.

24. Skjold A, Kristoffersen A, Vangberg TR, Haraldseth O, Jynge P, Larsson HB. An apparent unidirectional influx constant for manganese as a measure of myocardial calcium channel activity. *J Magn Reson Imaging* 2006; **24**; 5: 1047-1055.

25. Bloembergen N, Morgan LO. Proton Relaxation Times in Paramagnetic Solutions: Effects of Electron Spin Relaxation. *J Chem Phys* 1961; **34**: 842-850.

26. Roose P, Van Craen J, Andriessens G, Eisendrath H. NMR Study of Spin–Lattice Relaxation of Water Protons by Mn^{2+}Adsorbed onto Colloidal Silica. *Journal of Magnetic Resonance, Series A* 1996; **120**; 2: 206-213.

27. Stephens EM, Grisham CM. Lithium-8 Nuclear Magnetic Resonance, water proton nuclear magnetic resonance, and gadolinium electron paramagnetic resonance studies of the sarcoplasmic reticulum calcium ion transport adenosine triphosphatase. *Biochemistry* 1979; **18**: 4876-4885.

28. Tofts P. Quantitative MRI of the Brain: Measuring Changes by Disease: Wiley; 2003.

29. Lauterbur PC. Image Formation by Induced Local Interactions: Examples Employing Nuclear Magnetic Resonance. *Nature* 1973; **242**: 190-191.

30. Bers DM. Calcium fluxes involved in control of cardiac myocyte contraction. *Circulation research* 2000; **87**; 4: 275-281.

31. Pogwizd SM, Schlotthauer K, Li L, Yuan W, Bers DM. Arrhythmogenesis and contractile dysfunction in heart failure: Roles of sodium-calcium exchange, inward rectifier potassium current, and residual beta-adrenergic responsiveness. *Circulation research* 2001; **88**; 11: 1159-1167.

32. Saeed M. New concepts in characterization of ischemically injured myocardium by MRI. *Experimental biology and medicine (Maywood, NJ* 2001; **226**; 5: 367-376.

33. Taylor AM, Panting JR, Keegan J, Gatehouse PD, Amin D, Jhooti P, Yang GZ, McGill S, Burman ED, Francis JM, Firmin DN, Pennell DJ. Safety and preliminary findings with the intravascular contrast agent NC100150 injection for MR coronary angiography. *J Magn Reson Imaging* 1999; **9**; 2: 220-227.

34. Szolar DH, Saeed M, Wendland MF, Sakuma H, Roberts TP, Stiskal MA, Derugin N, Higgins CB. MR imaging characterization of postischemic myocardial dysfunction ("stunned myocardium"): relationship between functional and perfusion abnormalities. *J Magn Reson Imaging* 1996; **6**; 4: 615-624.

35. Kim RJ, Fieno DS, Parrish TB, Harris K, Chen EL, Simonetti O, Bundy J, Finn JP, Klocke FJ, Judd RM. Relationship of MRI delayed contrast enhancement to irreversible injury, infarct age, and contractile function. *Circulation* 1999; **100**; 19: 1992-2002.

36. Yu X, Zou J, Babb JS, Johnson G, Sanes DH, Turnbull DH. Statistical mapping of sound-evoked activity in the mouse auditory midbrain using Mn-enhanced MRI. *NeuroImage* 2008; **39**; 1: 223-230.

37. van der Zijden JP, Wu O, van der Toorn A, Roeling TP, Bleys RL, Dijkhuizen RM. Changes in neuronal connectivity after stroke in rats as studied by serial manganese-enhanced MRI. *NeuroImage* 2007; **34**; 4: 1650-1657.

38. Pautler RG, Silva AC, Koretsky AP. In vivo neuronal tract tracing using manganese-enhanced magnetic resonance imaging. *Magn Reson Med* 1998; **40**; 5: 740-748.

39. Weng JC, Chen JH, Yang PF, Tseng WY. Functional mapping of rat barrel activation following whisker stimulation using activity-induced manganese-dependent contrast. *NeuroImage* 2007; **36**; 4: 1179-1188.

40. Lin YJ, Koretsky AP. Manganese ion enhances T_1-weighted MRI during brain activation: an approach to direct imaging of brain function. *Magn Reson Med* 1997; **38**; 3: 378-388.

41. Van Meir V, Pavlova D, Verhoye M, Pinxten R, Balthazart J, Eens M, Van der Linden A. In vivo MR imaging of the seasonal volumetric and functional plasticity of song control nuclei in relation to song output in a female songbird. *NeuroImage* 2006; **31**; 3: 981-992.

42. Chen W, Tenney J, Kulkarni P, King JA. Imaging unconditioned fear response with manganese-enhanced MRI (MEMRI). *NeuroImage* 2007; **37**; 1: 221-229.

43. Minoshima S, Cross D. In vivo imaging of axonal transport using MRI: aging and Alzheimer's disease. *European journal of nuclear medicine and molecular imaging* 2008; **35 Suppl 1**: S89-92.

44. Smith KD, Kallhoff V, Zheng H, Pautler RG. In vivo axonal transport rates decrease in a mouse model of Alzheimer's disease. *NeuroImage* 2007; **35**; 4: 1401-1408.

45. Aoki I, Takahashi Y, Chuang KH, Silva AC, Igarashi T, Tanaka C, Childs RW, Koretsky AP. Cell labeling for magnetic resonance imaging with the T_1 agent manganese chloride. *NMR in biomedicine* 2006; **19**; 1: 50-59.

46. Gimi B, Leoni L, Oberholzer J, Braun M, Avila J, Wang Y, Desai T, Philipson LH, Magin RL, Roman BB. Functional MR microimaging of pancreatic beta-cell activation. *Cell transplantation* 2006; **15**; 2: 195-203.

47. Skjold A, Amundsen BH, Wiseth R, Stoylen A, Haraldseth O, Larsson HB, Jynge P. Manganese dipyridoxyl-diphosphate (MnDPDP) as a viability marker in patients with myocardial infarction. *J Magn Reson Imaging* 2007; **26**; 3: 720-727.

48. Saeed M, Higgins CB, Geschwind JF, Wendland MF. T_1-relaxation kinetics of extracellular, intracellular and intravascular MR contrast agents in normal and acutely reperfused infarcted myocardium using echo-planar MR imaging. *European radiology* 2000; **10**; 2: 310-318.

49. Wendland MF, Saeed M, Lund G, Higgins CB. Contrast-enhanced MRI for quantification of myocardial viability. *J Magn Reson Imaging* 1999; **10**; 5: 694-702.

50. Bremerich J, Saeed M, Arheden H, Higgins CB, Wendland MF. Normal and infarcted myocardium: differentiation with cellular uptake of manganese at MR imaging in a rat model. *Radiology* 2000; **216**; 2: 524-530.

51. Hu TC, Bao W, Lenhard SC, Schaeffer TR, Yue TL, Willette RN, Jucker BM. Simultaneous assessment of left-ventricular infarction size, function and tissue viability in a murine model of myocardial infarction by cardiac manganese-enhanced magnetic resonance imaging (MEMRI). *NMR in biomedicine* 2004; **17**; 8: 620-626.

52. Hu TC, Christian TF, Aletras AH, Taylor JL, Koretsky AP, Arai AE. Manganese enhanced magnetic resonance imaging of normal and ischemic canine heart. *Magn Reson Med* 2005; **54**; 1: 196-200.

53. Skjold A, Vangberg TR, Kristoffersen A, Haraldseth O, Jynge P, Larsson HB. Relaxation enhancing properties of MnDPDP in human myocardium. *J Magn Reson Imaging* 2004; **20**; 6: 948-952.

54. Greger JL. Dietary standards for manganese: overlap between nutritional and toxicological studies. *The Journal of nutrition* 1998; **128**; 2 Suppl: 368S-371S.

55. Brurok H, Schjott J, Berg K, Karlsson JO, Jynge P. Effects of manganese dipyridoxyl diphosphate, dipyridoxyl diphosphate--, and manganese chloride on cardiac function. An experimental study in the Langendorff perfused rat heart. *Investigative radiology* 1995; **30**; 3: 159-167.

56. Damadian R. Tumor detection by nuclear magnetic resonance. *Science (New York, NY* 1971; **171**; 976: 1151-1153.

57. Mansfield P, Maudsley AA. Line scan proton spin imaging in biological structures by NMR. *Physics in medicine and biology* 1976; **21**; 5: 847-852.

58. Mansfield P, Morris PG, Ordidge RJ, Pykett IL, Bangert V, Coupland RE. Human whole body imaging and detection of breast tumours by n.m.r. *Phil Trans R Soc Lond B* 1980; **289**: 503-510.

59. Chuang KH, Koretsky A. Improved neuronal tract tracing using manganese enhanced magnetic resonance imaging with fast T_1 mapping. *Magn Reson Med* 2006; **55**; 3: 604-611.

60. Shah NJ, Neeb H, Zaitsev M, Steinhoff S, Kircheis G, Amunts K, Haussinger D, Zilles K. Quantitative T_1 mapping of hepatic encephalopathy using magnetic resonance imaging. *Hepatology (Baltimore, Md* 2003; **38**; 5: 1219-1226.

61. Lee JH, Silva AC, Merkle H, Koretsky AP. Manganese-enhanced magnetic resonance imaging of mouse brain after systemic administration of $MnCl_2$: dose-dependent and temporal evolution of T_1 contrast. *Magn Reson Med* 2005; **53**; 3: 640-648.

62. Look DC, Locker DR. Nuclear Spin-Lattice Relaxation Measurements by Tone-Burst Modulation. *Physical Review Letters* 1968; **20**; 18: 987-989.

63. Look DC, Locker DR. Time Saving in Measurement of NMR and EPR Relaxation Times. *The Review of Scientific Instruments* 1970; **41**; 2: 250-251.

64. Crawley AP, Henkelman RM. A comparison of one-shot and recovery methods in T_1 imaging. *Magn Reson Med* 1988; **7**; 1: 23-34.

65. Brix G, Schad LR, Deimling M, Lorenz WJ. Fast and precise T_1 imaging using a TOMROP sequence. *Magnetic resonance imaging* 1990; **8**; 4: 351-356.

66. Steinhoff S, Zaitsev M, Zilles K, Shah NJ. Fast T_1 mapping with volume coverage. *Magn Reson Med* 2001; **46**; 1: 131-140.

67. Frahm J, Haase A, Matthaei D. Rapid NMR imaging of dynamic processes using the FLASH technique. *Magn Reson Med* 1986; **3**; 2: 321-327.

68. Loening AM, Gambhir SS. AMIDE: a free software tool for multimodality medical image analysis. *Mol Imaging* 2003; **2**; 3: 131-137.

69. Ni Y, Petre C, Bosmans H, Miao Y, Grant D, Baert AL, Marchal G. Comparison of manganese biodistribution and MR contrast enhancement in rats after intravenous injection of MnDPDP and MnCl2. *Acta Radiol* 1997; **38**; 4 Pt 2: 700-707.

70. Shigekawa M, Iwamoto T. Cardiac Na^+-Ca^{2+} exchange: molecular and pharmacological aspects. *Circulation research* 2001; **88**; 9: 864-876.

71. Federle MP, Chezmar JL, Rubin DL, Weinreb JC, Freeny PC, Semelka RC, Brown JJ, Borello JA, Lee JK, Mattrey R, Dachman AH, Saini S, Harmon B, Fenstermacher M, Pelsang RE, Harms SE, Mitchell DG, Halford HH, Anderson MW, Johnson CD, Francis IR, Bova JG, Kenney PJ, Klippenstein DL, Foster GS, Turner DA. Safety and efficacy of mangafodipir trisodium (MnDPDP) injection for hepatic MRI in adults: results of the U.S. multicenter phase III clinical trials (safety). *J Magn Reson Imaging* 2000; **12**; 1: 186-197.

72. Eriksson R, Johansson L, Bjerner T, Briley Saebo K, Ahlstrom H. Uptake of $MnCl_2$ and mangafodipir trisodium in the myocardium: a magnetic resonance imaging study in pigs. *J Magn Reson Imaging* 2004; **19**; 5: 564-569.

73. Krombach GA, Saeed M, Higgins CB, Novikov V, Wendland MF. Contrast-enhanced MR delineation of stunned myocardium with administration of $MnCl_2$ in rats. *Radiology* 2004; **230**; 1: 183-190.

74. Storey P, Chen Q, Li W, Seoane PR, Harnish PP, Fogelson L, Harris KR, Prasad PV. Magnetic resonance imaging of myocardial infarction using a manganese-based contrast agent (EVP 1001-1): preliminary results in a dog model. *J Magn Reson Imaging* 2006; **23**; 2: 228-234.

75. Corretti MC, Koretsune Y, Kusuoka H, Chacko VP, Zweier JL, Marban E. Glycolytic inhibition and calcium overload as consequences of exogenously generated free radicals in rabbit hearts. *The Journal of clinical investigation* 1991; **88**; 3: 1014-1025.

76. Camelliti P, Devlin GP, Matthews KG, Kohl P, Green CR. Spatially and temporally distinct expression of fibroblast connexins after sheep ventricular infarction. *Cardiovascular research* 2004; **62**; 2: 415-425.